Efficient ISAR image classification using MECSM representation

Valli Kumari Vatsavayi, Hari Kishan Kondaveeti [*]

Department of CS & SE, AUCE (A), Andhra University, Visakhapatnam, India

Abstract In this paper an efficient ISAR image classification method is proposed based on Minimum Enclosed Circle based Shape Matrix (MECSM) representation of the targets. Initially, discordant ISAR images are processed to remove the noise and outliers. Next, an orientation alignment method is used to align the targets vertically to achieve rotation invariance. The Enhanced Minimum Enclosed Circle calculation method (EnMEC) finds the radius and centre of the Minimum Enclosed Circle (MEC) of the shape. Then, the classification of the targets is performed based on shape matrices generated by the MECSM representation method proposed in this paper. The MECSM representation overcomes the limitations of the conventional shape matrix representation such as the dependency of the shape matrix representation on centre of mass (COM) and maximum radius of the shape of the target. The MECSM representation also curtails the extraneous interpolations in representing the insignificant details around the target. Experimental analysis shows that the proposed method is robust against the deformations in the rudimentary silhouettes of the targets emanated from the complications abounded with ISAR image reconstruction and processing mechanisms.

© 2016 The Authors. Production and hosting by Elsevier B.V. on behalf of King Saud University. This is an open access article under the CC BY-NC-ND license (http://creativecommons.org/licenses/by-nc-nd/4.0/).

1. Introduction

Inverse Synthetic Aperture Radar (ISAR) is an active imaging radar, used in military surveillance and maritime patrolling in hostile environments to generate the images of targets in almost all weather conditions, day and night, where optical imaging technologies fail utterly (Chen and Anderson, 1980; Chen, 2014; Nuthalapati, 1992; Ozdemir, 2012; Tang et al., 2012; Zeljkovic et al., 2010). ISAR has the capability of reconstructing the images of targets moving in a non-cooperative way. Motion of the targets is instrumental in ISAR image reconstruction where it produces blur effect in case of other imaging radars.

ISAR imagery represents the two dimensional map of the target reflectivity synthesized from the reflected signal from a target (Chen and Anderson, 1980; Kozma et al., 1984). The shape of a target in the ISAR image is generated by the cross product of the line of sight (LOS) vector with the instanta-

* Corresponding author.
  E-mail addresses: vallikumari@gmail.com (V.K. Vatsavayi), kishan.kondaveeti@gmail.com (H.K. Kondaveeti).
Peer review under responsibility of King Saud University.

neous angular velocity vector of the target. Fig. 1 shows the ISAR images of different aircrafts at arbitrary aspect angles.

The features of ISAR imagery are very effective in identifying the radar targets such as aircrafts, battle ships, guided missiles and military vehicles than that of the imagery of other imaging radars existing today. But, however, the following impediments are making the classification of targets from ISAR imagery challenging. (i) ISAR images are quite different from optical images and are usually much more difficult to understand (Brett, 1997; Skinner et al., 1998; Sullivan, 2000); (ii) ISAR images have severe and unavoidable geometric distortion compared with optical images; (iii) ISAR images do not contain rational information such as colour and texture of the target surface which is crucial for target discrimination and classification; (iv) ISAR images are highly susceptible to noise due to multiple bounce scattering from external surfaces, coarse nature of the target surfaces and internal motions. Noise and clutter present in the images result in poor signal-to-noise ratio (SNR) and low signal-to-clutter ratio (SCR); (v) Blur, discontinuities and deformations often associate with ISAR images due to complications abounded with image reconstruction and processing mechanisms. These problems degrade the overall performance of the classification significantly.

Classification of ISAR targets (Bachmann et al., 1992; Botha, 1994; Kondaveeti and Vatsavayi, 2016; Kim et al., 2005; Maki et al., 2001; Musman et al., 1996; Rosenbach and Schiller, 1995; Saidi et al., 2009; Park et al., 2015) is a popular concept in the literature as it is difficult to implement the automated classification systems for practical operational purposes. Template matching is the simplest technique for target classification (Jain et al., 2000) which determines the matching between Range or Doppler profiles. The methods described in Bachmann et al. (1992), Maki et al. (2001) and Musman et al. (1996) mainly deal with classification of ship targets from ISAR images. They can not be applied directly to other types of targets such as aircrafts because they rely on 3D models of the ships to extract the silhouette parameters such as length of the ship, position and height of main mast etc.

Botha (1994), Kondaveeti and Vatsavayi (2016), Kim et al. (2005), Rosenbach and Schiller (1995), Saidi et al. (2009) and Park et al. (2015) deal with the 2D ISAR aircraft target classification. The methods described in Botha (1994), Rosenbach and Schiller (1995) and Saidi et al. (2009) are based upon the low dimensional local and geometric characteristics of an ISAR image such as geometrical moments, shape features, quantized energy features, zernike moments and moment invariants. They tried to simplify the classifier structure in order to save the computational resources. But these features are less discriminative and may not be successful always. Kim et al. (2005) described a polar mapping method for the classification of aircrafts. It relies on three step classifier consisting of a coarse search, fine search and alignment, and final decision. This method is computationally expensive because of the complexity involved in representing the images in polar form and its complex classifier structure. This method assumes that Centre Of Mass (COM) and Rotation Centre (RC) are same for the targets in the generated images, which is not possible always. The method (Park et al., 2015) uses the polar mapping of Fourier magnitude images to achieve the translation, rotation and scale invariant features. This method addresses the problem of having COM and RC different by 2D-Fourier Transform (2D-FT), as 2D-FT determines RC as zero-frequency point automatically. But, this method adds overheads in transforming the images between spatial and frequency domains. The accuracy of this method is questionable in case of variations in pixel intensity values due to low SNR, deformations in the shape of the targets and blur. The method proposed in Kondaveeti and Vatsavayi (2016) depends on the shape matrices (Goshtasby, 1985; Taza and Suen, 1989). The dependency of this method on the shape details of the targets rather than the true scatter responses of the target in the 2D-image plane makes it sturdy. But, however, this method fails mostly in case of deformations and discontinuities in the shape of the targets as the shape representation mechanism developed in this method depends on the COM and maximum radius of the shape. The accuracy of this method is biased with
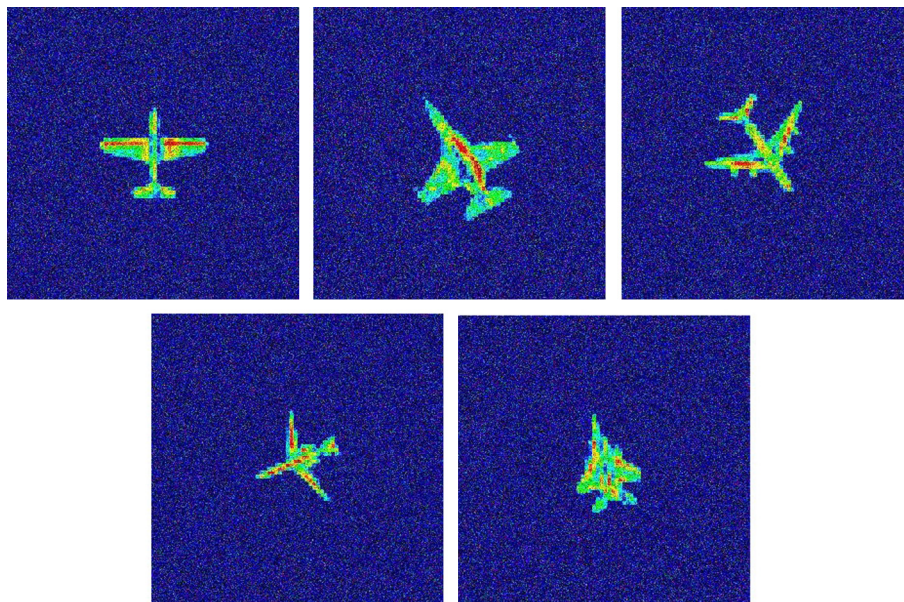

Figure 1   ISAR images of different aircrafts at arbitrary aspect angles.

the variations in the COM and maximum radius caused by the deformations and discontinuities in the shape of the target.

In this paper, the work is aimed at the development of effective target classification method which is robust against the deformations and discontinuities in the shape of the target. We proposed a new classification method based on MECSM representation of the targets. The MECSM representation of a target is the low dimensional, concise representation of geometrical shape of the targets and is invariant to translation, rotation and scale. The proposed MECSM representation method depends on the Minimum Enclosed Circle (MEC) of the scatter responses that represent the targets in 2D ISAR imagery.

Our contributions in this work are: (i) the development of a target vertical alignment method to achieve rotation invariance in MECSM representation of targets based on Jaccard distance metric. (ii) the development of an improvised method, Enhanced Minimum Enclosed Circle calculation method (EnMEC), to calculate centre and radius of MEC. (iii) the development of new ISAR image classification scheme based on MECSM representation method.

Basic geometry involved in the construction of MEC is explained in Section 2. The detailed description of the proposed classification algorithm is presented in Section 3. Section 4 contains the experimental analysis and associated discussions on the performance of proposed method on synthesized ISAR image database. The work is concluded in Section 5.

2. Basic geometry

Let $P = \{P_1, P_2, P_3, \ldots, P_n\}$ is a finite set of n points given in 2-dimensional Euclidean space, $P \in \mathbb{R}^2$ and (x_1, y_1), $(x_2, y_2) \ldots (x_n, y_n)$ are the coordinates of the points $P_1, P_2 \ldots P_n$ respectively.

2.1. Law of cosines

The law of cosines relates the lengths of the sides of a triangle to the cosine of one of its angles. This law is to find the length of a side or size of an angle. According to this law, for a triangle formed with any three points $P_i(x_i, y_i)$, $P_j(x_j, y_j)$ and $P_k(x_k, y_k)$ in the set $P \in \mathbb{R}^2$ having angles α, β and γ at vertices P_i, P_j and P_k respectively. The size of the angles α, β and γ can be calculated from the Eqs. (1)–(3) respectively.

$$\alpha = \cos^{-1}\left(\frac{p_2^2 + p_3^2 - p_1^2}{2p_2p_3}\right) \tag{1}$$

$$\beta = \cos^{-1}\left(\frac{p_3^2 + p_1^2 - p_2^2}{2p_3p_1}\right) \tag{2}$$

$$\gamma = \cos^{-1}\left(\frac{p_1^2 + p_2^2 - p_3^2}{2p_1p_2}\right) \tag{3}$$

where p_1, p_2 and p_3 are the lengths of the sides P_jP_k, P_kP_i and P_iP_j respectively. Lengths of the sides p_1, p_2 and p_3 can be calculated using the Eqs. (4)–(6)

$$p_1 = \sqrt{(x_j - x_k)^2 + (y_j - y_k)^2} \tag{4}$$

$$p_2 = \sqrt{(x_k - x_i)^2 + (y_k - y_i)^2} \tag{5}$$

$$p_3 = \sqrt{(x_i - x_j)^2 + (y_i - y_j)^2} \tag{6}$$

2.2. Circumscribed circle

For a triangle formed with any three points $P_i(x_i, y_i)$, $P_j(x_j, y_j)$ and $P_k(x_k, y_k)$ in the set $P \in \mathbb{R}^2$, Circumscribed circle or Circumcircle is a circle that passes through all the vertices of the triangle. The centre of this circle is called the Circumcentre and its radius is called the Circumradius.

The centre of the circle (Circumcentre) passes through the points P_i, P_j and P_k can be calculated from Eq. (7)

$$(C_x, C_y) = \left(\frac{a_1b_1 - a_2b_2}{2b_3}, \frac{a_3b_2 - a_4b_1}{2b_3}\right) \tag{7}$$

where C_x and C_y are the x and y coordinates of the centre of the circle (Circumcentre) and

$$\begin{aligned}
a_1 &= y_k - y_i & a_1' &= y_k + y_i \\
a_2 &= y_j - y_i & a_2' &= y_j + y_i \\
a_3 &= x_j - x_i & a_3' &= x_j + x_i \\
a_4 &= x_k - x_i & a_4' &= x_k + x_i \\
a_5 &= y_k - y_j & a_5' &= x_k - x_j
\end{aligned}$$

$$b_1 = a_3a_3' + a_2a_2'$$
$$b_2 = a_4a_4' + a_1a_1'$$
$$b_3 = a_3a_5 - a_2a_5'$$

To check the collinearity of the given three points, the term b_3 in Eq. (7) should be calculated. If the three points are collinear, the value of the term b_3 is equal to zero and they can not define a circle. otherwise, the three points can define a circle.

Once the centre of the circle is calculated, the radius r_{circum} of the circle (Circumradius) can be calculated from Eq. (8)

$$r_{circum} = \sqrt{(x_p - C_x)^2 + (y_p - C_y)^2} \tag{8}$$

where x_p and y_p are the x and y coordinates of a point on the circle.

2.3. Minimum Enclosing Circle (MEC)

Minimum Enclosing circle (MEC) is the smallest radius circle that encloses all the points P_1, $P_2 \ldots P_n$ in the set $P \in \mathbb{R}^2$. In the case of a polygon formed with n points P_1, $P_2 \ldots P_n$ in the set $P \in \mathbb{R}^2$, Minimum Enclosing Circle (MEC) is the smallest circle that completely contains the polygon within it.

The following properties of MEC are crucial in finding the MEC of a given set of points:

(i) The MEC of the finite set $P \in \mathbb{R}^2$ is unique.
(ii) The MEC of the finite set $P \in \mathbb{R}^2$ can be determined by either two or three points in P.
(iii) If MEC is determined by three points in P, then the triangle formed by that points is always an acute or right angled i.e. maximum angle in the triangle is always less than or equal to 90°.

MEC is different from Circum Circle. Every polygon has a unique MEC and every polygon may not have a circumscribed circle i.e. all the vertices of the given polygon do not need to lie on a circle.

3. Proposed classification method

3.1. Preprocessing

ISAR images are heavily corrupted by noise and clutter. They must be processed before extracting the features in order to increase the accuracy of the classification. Preprocessing involves in noise reduction, and orientation alignment. The following sub-sections explain the preprocessing procedure briefly.

3.1.1. Noise reduction

Speckle or Granular noise is generally associated with the radar generated images. Speckle noise is multiplicative in nature. However, the filters that deal with the additive noise are not suitable to deal with this noise. The segmentation using the global mean is the simple and effective method to handle this noise (Franceschetti and Lanari, 1999; Kim et al., 2005; Park et al., 2015) when SNR and SCR are relatively high. Instead of using simple mean threshold, in the proposed method, the threshold value is selected based on grey level histograms (Otsu, 1979) for the effective noise removal even in case of low SNR. To determine the optimal threshold value ζ, it is assumed that the image I contains two classes of pixels i.e. foreground and background and follows the bi-modal histogram. Next, the threshold value is calculated by minimizing their intra-class variance or maximizing inter-class variance. The processed image I' using the obtained threshold ζ is represented as in Eq. (9).

$$I' = \begin{cases} 1 & \text{if } I > \zeta \\ 0 & \text{if } I \leqslant \zeta \end{cases} \tag{9}$$

The image pixels whose intensity values exceed the given threshold, ζ are considered as 1 and the remaining pixels are set to zero. As the texture information does not carry any useful information for the target discrimination in case of ISAR images all the grey level intensity values above the given threshold are converted to 1 to obtain a black and white image.

Most of the times, some outliers still remain in the images even after performing the thresholding, due to the limitations in the automated global threshold selection in the previous step. Outliers are some connected components located at far-flung corners of the image which do not belong to the actual shape of the target. The outliers must be removed as they adversely affect the generation of MEC. Area opening operation alleviates the affect of the outliers by removing the connected components with area smaller than a given parameter λ.

Let us consider the image I' as a set of connected components and $\lambda \geqslant 0$ then the area opening, γ^a of I' at given parameter λ is defined as in the following Eq. (10):

$$\gamma_\lambda^a(I') = \{x \in I' | Area(C_x(I')) \geqslant \lambda\} \tag{10}$$

where $C_x(I')$ is the connected component of the image I' at point x.

The image obtained after performing area opening on I' can be expressed as in Eq. (11)

$$I'' = \gamma_\lambda^a(I') \tag{11}$$

The values of global threshold ζ and parameter λ of area opening operation play vital role in removing the unwanted details by preserving the discriminative information for the classification. Improper selection of values may cause discontinuities and deformations in the shape of the target. Hence, care must be taken while selecting the optimal values. Further investigation is required for the optimal selection of these values. After noise reduction, the processed image I'' is passed to the next stage.

3.1.2. Orientation alignment

To achieve rotation invariance in the shape matrix representation, existing method (Goshtasby, 1985) considers the maximum radius of the shape of a target as the cardinal radial line to initialize representation. However, the dependency of the shape matrix representation on the maximum radius of the shape of a target may bias the classifier accuracy as the variation in the maximum radius due to deformations in the shape of a target can cause variations in the shape matrix representation. The proposed method does not consider the maximum radius of the shape of a target to initialize the shape matrix representation. Instead, it aligns all the targets towards a particular orientation and then initiates the shape matrix representation from a radial line oriented $0°$ w.r.t horizontal axis. To align the targets towards a particular orientation, a target alignment method is developed based on Jaccard distance metric (Jaccard, 1901). This method depends on the geometry of the shapes of the targets in the ISAR imagery to align them vertically. The advantage of the vertical mirror symmetry in the shape of the aircraft targets is considered as the crucial factor in vertical alignment. Following procedure explains the process of vertical alignment of targets:

Step 1. Initially, obtain the flopped image from the processed image I'' obtained from the previous stage. A flopped image is the mirror-reversal of original image across the vertical axis. I''_{flop} in Eq. (12) represents the flopped image obtained from I''.

$$I''_{flop} = Flip_{vertical}(I'') \tag{12}$$

Step 2. Calculate the Jaccard distance, $d_{Jaccard}(I'', I''_{flop})$ from the original image I'' and flopped image I''_{flop} as given in Eq. (13)

$$d_{Jaccard}(I'', I''_{flop}) = \frac{|I'' \cup I''_{flop}| - |I'' \cap I''_{flop}|}{|I'' \cup I''_{flop}|} \tag{13}$$

where $|I'' \cap I''_{flop}|$ and $|I'' \cup I''_{flop}|$ are the sum of all matches in the intersection and the union of the images I'' and I''_{flop} respectively. The value of the Jaccard distance, $d_{Jaccard}$ lies between 0 and 1. $d_{Jaccard}(I'', I''_{flop})$ approaches 0 if the shape of the target is oriented vertically. A threshold distance value nearer to zero is selected as the stopping criterion of the process.

Step 3. Check whether the Jaccard distance, $d_{Jaccard}$ obtained in the above step is less than or equal to the given threshold. If the condition is satisfied stop the procedure

and return the image, otherwise rotate the image I'' by $1°$ clockwise and repeat the steps (1), (2) and (3).

Fig. 2 depicts the images generated at different stages during the process of vertical alignment of targets. Fig. 2(a) and (e) are two input images. Target in (a) is oriented at some arbitrary angle with respect to vertical axis and target in (e) is vertically oriented i.e. $0°$ orientation with respect to vertical axis. Fig. 2(b), (c) and (d) represent flopped image of (a), intersection and union of two images (a) and (b) respectively. As the target is oriented at some arbitrary angle with vertical axis intersection and union of two images are different and $d_{Jaccard}$ is away from given threshold. This target must be rotated until $d_{Jaccard}$ approaches the given threshold as described in the above procedure. Fig. 2(f), (g) and (h) represent flopped image of (e), intersection and union of two images (e) and (f) respectively. As the target is vertically oriented already, intersection and union of two images are same and $d_{Jaccard}$ approaches given threshold. Rotation orientation need not be performed on the image (e).

The output obtained from this step, the vertically aligned image is passed to the next section.

3.2. MECSM representation

Let X be a finite set of connected components that represent a target in 2-dimensional Euclidean space, $X \in \mathbb{R}^2$ and X_i is a connected component in the set X where $X = \bigcup\{X_i | i = 1 : n\}$ where n is the number of connected components in the set X. In case of a target with no disjunctions in its shape, set X contains one connected component alone i.e. $X = X_1$. A connected component X_i represents a finite set of points and $|X_i|$ represents the cardinality of X_i. Let S_i represent a set of points that form the border of a connected component X_i and $|S_i|$ represent the cardinality of S_i where $S = \bigcup\{S_i | i = 1 : n\}$, S is a superset of all S_i's. Then, it is clear that $X \in \mathbb{R}^2$, $S \in \mathbb{R}^2$ and $S \subset X$. If l represents the total number of points in all the connected components in the set X and m represents the total number of border points of all the connected components in

the set S respectively then $l \gg m$ in general. $l \simeq m$ in worst case scenario where the shape of the target is heavily distorted by the disjunctions and discontinuities.

The complexity of finding the centre and radius of the MEC of a target increases with the number of points that represent the target i.e. computational complexity increases with l. Hence, to reduce the complexity of the MEC generation, we have chosen the set S that contains the boundary points of the connected components that form a target. The number of points are further reduced by finding the convex hull of S. Convex hull of S is a set of points that form a smallest convex region containing S.

### 3.2.1. Calculation of centre and radius of MEC using EnMEC

The proposed Enhanced Minimum Enclosed Circle calculation method (EnMEC) reduces the complexity of the method described in Gadelmawla (2010) by reducing the repetitive calculation of radii of the circles formed by selecting the three consecutive points from set of points in the convex hull for the removal of the points. The procedure for calculation of centre and radius of MEC using EnMEC is as follows:

Step 1. Count the number of connected components in the given image.
Step 2. If count is 1, then extract the boundary points of the given shape and move to step 3. Otherwise, extract the boundary points of each connected component that belongs to the given shape and move to step 3.
Step 3. Find the set of points $C = \{C_1, C_2, C_3, \ldots, C_n\}$ that form a convex hull for the given set of border points where n is the number of points in the convex hull and (x_1, y_1), $(x_2, y_2) \ldots (x_n, y_n)$ are the coordinates of the points C_1, $C_2 \ldots C_n$ respectively. Store every point C_i in the convex hull along with a unique id U_{id} from 1 to n i.e. $U_{id} = \{1, 2, 3, 4, \ldots, n - 2, n - 1, n\}$ in the lookup table LT to identify each point uniquely.
Step 4. Form n ordered combinations with every three successive unique id's of the points in the convex hull. For the first point, use unique id's of both the second and last
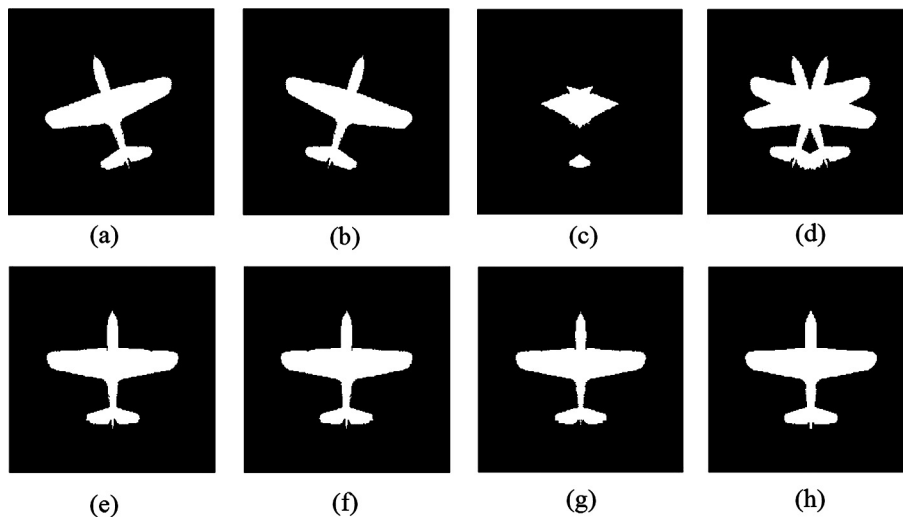
Figure 2 Performing orientation alignment on the preprocessed image. (a) Original image I'' at some arbitrary orientation; (b) Flop image I''_{flop} generated from I'; (c) Intersection image of (a) and (b); (d) Union image of (a) and (b); (e) Original image J'' at vertical orientation ($0°$ orientation); (b) Flop image J''_{flop} generated from J''; (c) Intersection image of (a) and (b); (d) Union image of (a) and (b).

points and for the last point, use unique id's of both the last but one and first points in the convex hull. For example, in the first iteration, ordered combinations formed by three successive unique id's of n points in the convex hull are $\{\{1, 2, 3\}, \{2, 3, 4\}, \ldots, \{n - 1, n, 1\}, \{n, 1, 2\}\}$.

Step 5. Create a matrix M of size $n \times 2$. In each row of matrix M, first column holds the combination of three successive unique id's from the lookup table LT and the second column holds the value of the radius of the circle passing through the three points corresponding to the combination of unique id's in the first column of the same row. Initially, fill first column of each row with a combination of three successive unique id's from the lookup table LT and fill all the elements of second column of each row with zero.

Step 6. For each row of the matrix M containing a unique ordered combination, if the radius value is not calculated i.e. value in the second column of the respective row is zero then find the points corresponding to the unique id's of the ordered combination and calculate the radius of the circle passing through the three points using the Eqs. (7) and (8) and save the value in the second column of the respective row of the matrix M. Otherwise, move to next row. For example, consider radii values for the combination of unique id's $\{1, 2, 3\}, \{2, 3, 4\}, \ldots, \{n - 3, n - 2, n - 1\}$, $\{n - 2, n - 1, n\}, \{n - 1, n, 1\}$ and $\{n, 1, 2\}$ as 100, 98, ..., 97, 105, 96 and 102 respectively. The radius value 105 belongs to the combination of unique id's $\{n - 2, n - 1, n\}$ is considered as the maximum value.

Step 7. Find the combination $\{a, b, c\}$ where a, b and c belongs to U_{id} and $1 \leqslant a, b, c \leqslant n$ with the radius value maximum. Remove the middle unique id b and the point corresponding to the unique id C_b from the convex hull and remove the rows containing the combinations with unique id b from the matrix M. From the above example, the radius value is maximum for the combination $\{n - 2, n - 1, n\}$. Hence, the unique id $n - 1$ and the point corresponding to the unique id C_{n-1} should be removed from the lookup table LT and the rows containing the combinations of unique id's with the unique id $n - 1$ should also be removed from the matrix M. The rows containing the combination of unique id's with the unique id $n - 1$

($\{n - 3, n - 2, n - 1\}$, $\{n - 2, n - 1, n\}$ and $\{n - 1, n, 1\}$) in the matrix M and the row containing the unique id $n - 1$ in the lookup table LT are highlighted in Fig. 3. The lookup table LT and matrix M are updated by removing the highlighted rows.

Step 8. After updating the lookup table LT, form ordered combinations with every three successive unique id's of the points in the lookup table LT again as in step 4.

Step 9. For every new combination of the unique id's, check whether the combination exist in the matrix M or not. If a combination does not exist in the matrix M add that combination to the matrix. Otherwise move to the next combination. Fig. 4 depicts the matrix M with updated rows having new combination of unique id's from the updated lookup table LT.

Step 10. Repeat steps 6, 7, 8 and 9 until only three points remain in the lookup table LT and single row in matrix M. The triangle formed by these three points is known as MEC triangle.

Step 11. Calculate the three angles of the MEC triangle using Eqs. (1)–(3) and find the largest one.

Step 12. If the largest angle is less than or equal to 90°, then calculate centre O_{MEC} and radius r_{MEC} of the MEC using the Eqs. (7) and (8) respectively. Otherwise, the MEC will be the diametric circle passing through the two end points of the largest side of the MEC triangle.

Fig. 5 depicts the centre O_{MEC} and radius r_{MEC} of the MEC obtained for an aircraft target using the EnMEC method. For example, (139,207), (196,173) and (139,96) are the three points that form MEC triangle. From the Eqs. (7) and (8), the O_{MEC} is (144.5,151.5) and r_{MEC} is 55.7753. These values are passed to the next step to obtain the shape matrix.

3.2.2. Shape matrix representation

To obtain the shape matrix of size $m \times n$, an imaginary polar grid having n concentric circles and m radial lines is constructed over the target and the intensity values are sampled from the intersection points of the radial lines and concentric circles as shown in Fig. 6(a) and (b). Fig. 6(a) contains a polar grid formed by 24 radial lines and 4 concentric circles i.e.
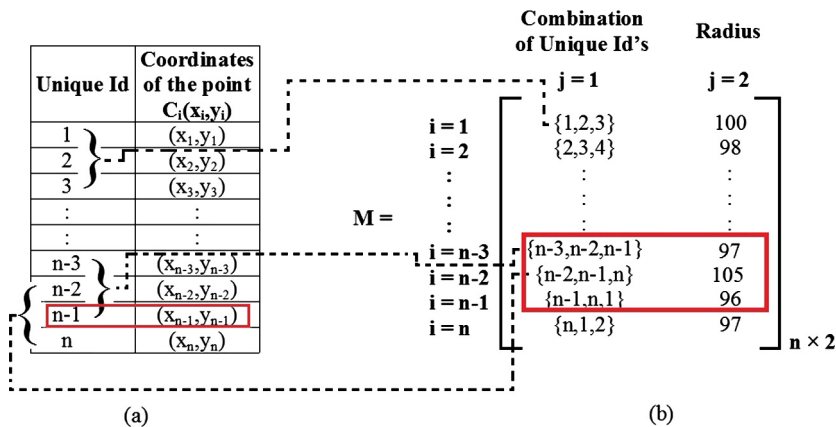
Figure 3 The lookup table LT and matrix M after the calculation of radii values. (a) Lookup table LT containing the points from the set C and their corresponding unique id's; (b) Matrix M containing the radii values in the second column of each row. The rows containing the combination of unique id's with the unique id $n - 1$ ($\{n - 3, n - 2, n - 1\}, \{n - 2, n - 1, n\}$ and $\{n - 1, n, 1\}$) in the matrix M and the row containing the unique id $n - 1$ in the lookup table LT are highlighted.

(a)   (b)
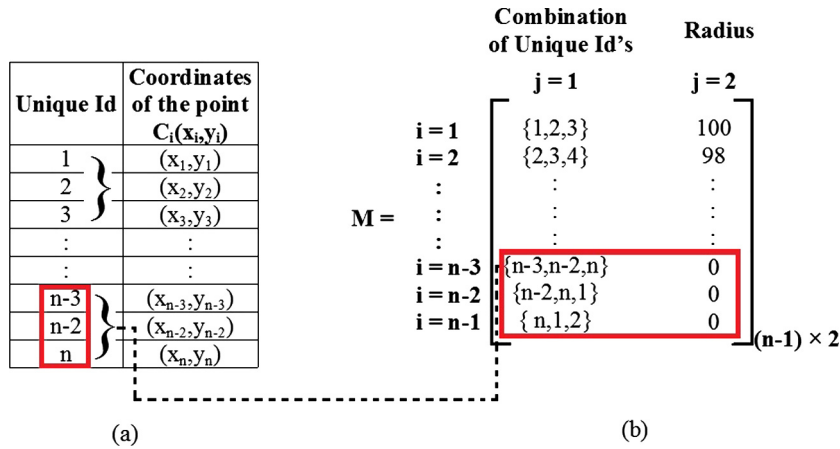
Figure 4 The updated lookup table LT and matrix M after first iteration. (a) Lookup table LT containing the remaining points from the set C and their corresponding unique id's after the deletion of a row; (b) Matrix M containing the updated rows with new combination of three successive unique id's from the lookup table LT.
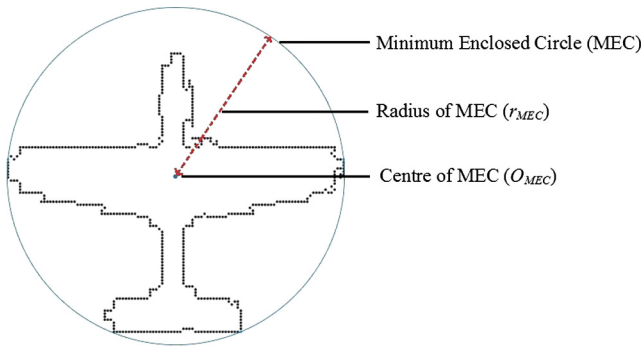
Figure 5 Centre and radius of the MEC obtained for an aircraft target using EnMEC method.

$m = 24$ and $n = 4$. r_{max} and r_{min} represent the radii of maximum and minimum sampling circles in the grid and d_θ and d_r represent the sampling intervals between radial lines and sampling circles respectively. Fig. 6(b) contains the shape matrix generated by the polar sampling of the shape details. Construction of shape matrix of size $m \times n$ from the centre O_{MEC} and radius r_{MEC} of the MEC is presented here briefly.

> Step 1. Construct n concentric circles with the radii $r_{MEC}/(n-1), 2r_{MEC}/(n-1), \ldots, (n-1)r_{MEC}/(n-1)$ having O_{MEC} as the centre.
> Step 2. Generate m equal arcs with an angle $(360/m)°$ to divide the n concentric circles into m radial lines.
> Step 3. Then, sample $m \times n$ pixels from the intersection points of the m radial lines and n concentric circles and fill the elements of the shape matrix with 1's if a sampled point belongs to the shape otherwise filled with 0's to form a shape matrix of size $m \times n$.

Fig. 6(c) depicts the imaginary polar grid constructed from 10 radial lines and 5 sampling circles laid over an aircraft target and Fig. 6(d) represents the shape matrix of size 10×5 obtained from polar quantization of the target. The size of shape matrix is considered as 10×5 arbitrarily for illustration purpose.

Fig. 7(a) and (b) depicts the imaginary polar grids generated by the existing (Goshtasby, 1985) and proposed methods respectively in the process of shape matrix generation. As discussed above, the generation of polar grid by the existing method (Goshtasby, 1985) depends on the COM and maximum radius of the shape. It causes the sampling of insignificant details around the object as shown in Fig. 7(a), which do not contribute any information for the target discrimination. The proposed method depends on the centre and radius of the MEC obtained by EnMEC calculation method to generate the polar grid which avoids the sampling of insignificant details around the target as shown in Fig. 7(b). As the polar quantization in the proposed method considers more influential details than the existing method using the same number of sampling points, the shape matrix generated by the proposed method is a more accurate representation of the target and is more discriminative.
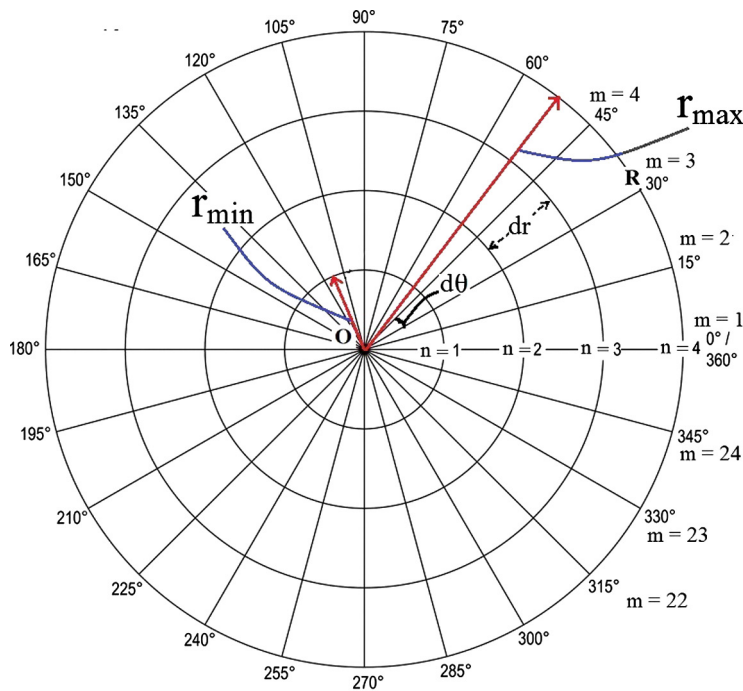
3.3. Classification

The proposed classification method follows the typical classification procedure which involves in construction of the training database and testing. Initially, the image dataset containing the ISAR images of aircraft targets is divided into training and testing data. In the training phase, images are selected from the training data to train the classifier. These images are pre-processed and their shape matrices are obtained using the proposed method and are stored in the database with their corresponding class labels. In the testing phase, rotated and down-scaled image is given as input. The test image is pre-processed and their shape matrices are obtained using the proposed method. Then, the similarity value is calculated between the shape matrices of test image and the trained images using the measure described in Eq. (14).

$$Similarity = 1 - \left[\frac{S}{mn}\right] \qquad (14)$$

where S is sum of all matches by performing $exclusiveOR$ (XOR) operation between the shape matrices obtained from the given two target images, m and n are the No. of rows and No. of columns of the shape matrices. The similarity value

$$\text{Shape Matrix, M} = \begin{array}{c} \\ m=1 \\ m=2 \\ \\ \\ m=23 \\ m=24 \end{array} \begin{array}{cccc} n=1 & n=2 & n=3 & n=4 \\ \left[\begin{array}{cccc} M_{1,1} & M_{1,2} & M_{1,3} & M_{1,4} \\ M_{2,1} & M_{2,2} & M_{2,3} & M_{2,4} \\ \cdot & \cdot & \cdot & \cdot \\ \cdot & \cdot & \cdot & \cdot \\ M_{23,1} & M_{23,2} & M_{23,3} & M_{23,4} \\ M_{24,1} & M_{24,2} & M_{24,3} & M_{24,4} \end{array}\right]_{24 \times 4} \end{array}$$

(a)

(b)

$$\text{Shape Matrix, M} = \begin{array}{c} \\ m=1 \\ m=2 \\ m=3 \\ m=4 \\ m=5 \\ m=6 \\ m=7 \\ m=8 \\ m=9 \\ m=10 \end{array} \begin{array}{ccccc} n=1 & n=2 & n=3 & n=4 & n=5 \\ \left[\begin{array}{ccccc} 1 & 1 & 1 & 1 & 1 \\ 1 & 0 & 0 & 0 & 0 \\ 1 & 0 & 0 & 0 & 0 \\ 1 & 1 & 0 & 0 & 0 \\ 1 & 1 & 0 & 0 & 0 \\ 1 & 1 & 1 & 1 & 1 \\ 1 & 1 & 0 & 0 & 0 \\ 1 & 0 & 0 & 1 & 0 \\ 1 & 0 & 0 & 1 & 0 \\ 1 & 1 & 0 & 0 & 0 \end{array}\right]_{10 \times 5} \end{array}$$

(c)

(d)

Figure 6 Polar quantization of an aircraft target to generate shape matrix. (a) Sample polar grid constructed from No. of radial lines, $m = 24$ and No. of concentric circles, $n = 4$; (b) Shape matrix derived by the polar quantization having No. of rows, $m = 24$ and No. of columns, $n = 4$; (c) polar grid over the aircraft image having No. of radial lines, $m = 10$ and No. of concentric circles, $n = 5$; (d) Shape matrix derived from the aircraft having No. of rows, $m = 10$ and No. of columns, $n = 5$.

lies between 0 and 1. If the similarity value between the shape matrices of two images approaches zero the two images are dissimilar and if the value is close to 1 the images are most similar.

The class label of the given test image is determined as the class label of the trained image with which the maximum similarity value is obtained. Fig. 8 depicts the overall description of the proposed classification method.

4. Experimental results

Experimental analysis is carried out to compare the performance of the proposed method against the conventional classification method, polar mapping method (Kim et al., 2005) and 2D-Fourier transform based polar mapping method (Park et al., 2015). The conventional classification method is Euclidean distance based and the method described in Kim
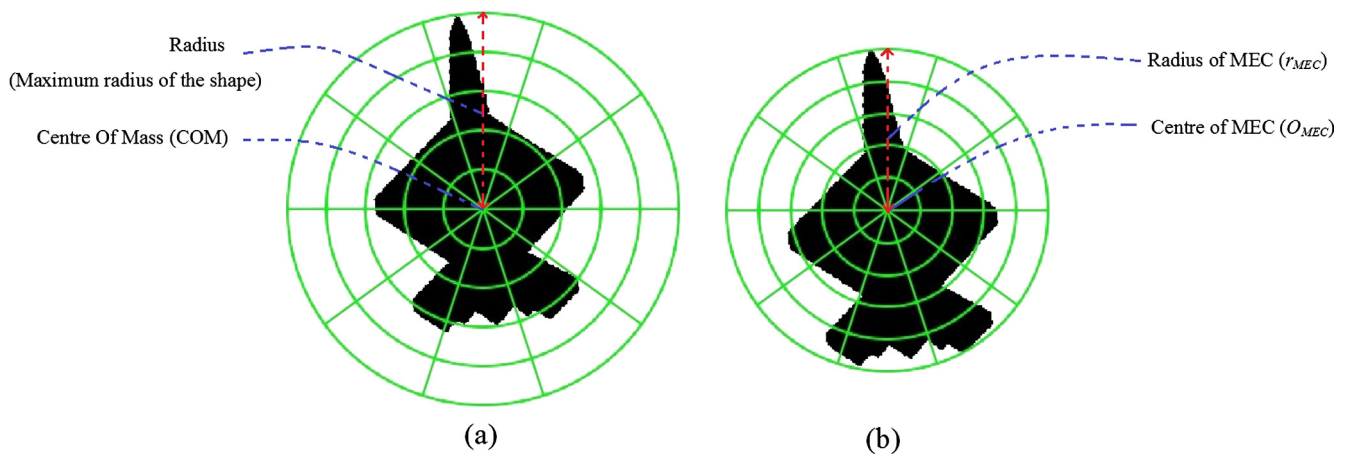
Figure 7 Comparison of imaginary polar grids generated in the process of shape matrix generation. (a) imaginary polar grid generated by existing (Goshtasby, 1985) having COM as centre and Maximum radius of the shape as the radius (b) imaginary polar grid generated by proposed method having centre of minimum enclosed circle O_{MEC} as centre and radius of minimum enclosed circle r_{MEC} as the radius.
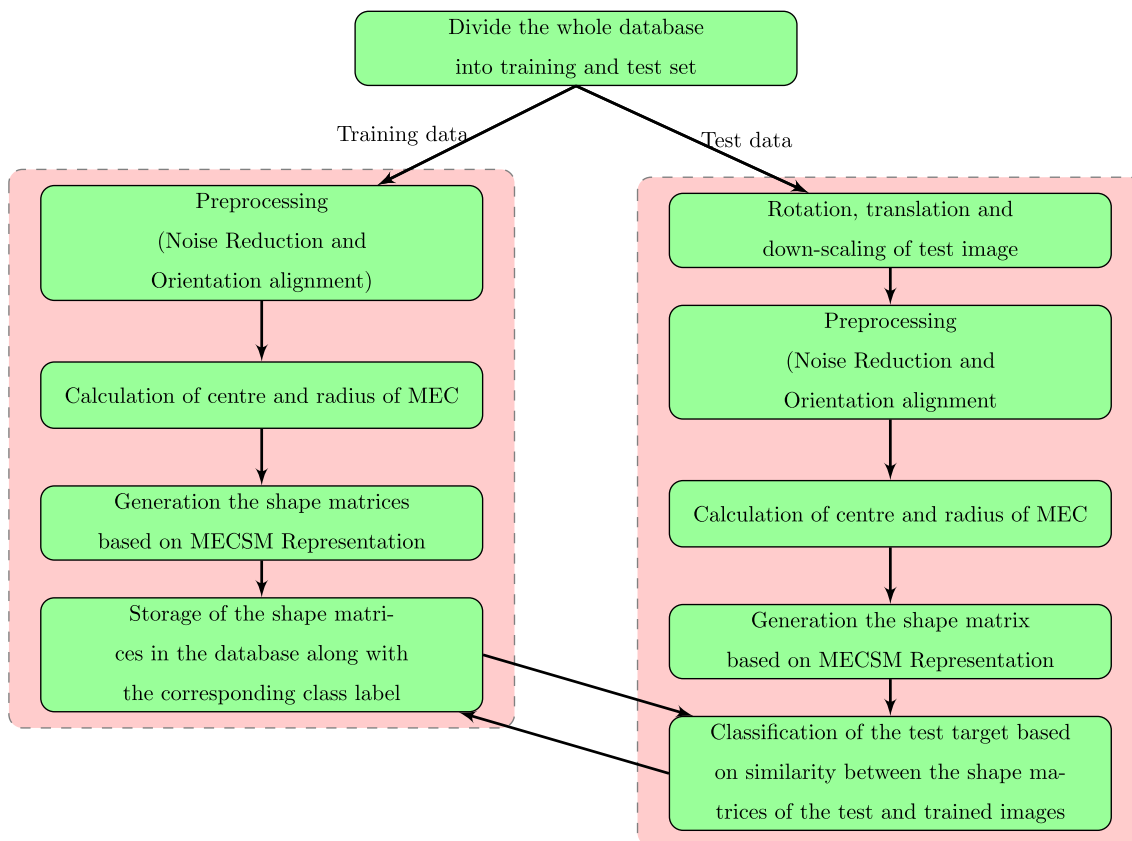
Figure 8 Overall description of the proposed classification method.

et al. (2005) is based on the polar mapping of the ISAR images from cartesian domain to (r, θ). Polar mapping of the images is invariant to translation. Rotational invariance is achieved by the conversion of the rotation to translation. This method assumes that RC and COM are same. Classifier proposed in this method depends on three level decision system to reduce the search space. In this method, the classifier decision depends on the number of samples selected η and γ in the coarse and fine search phases. As there is no predefined method to choose the optimal threshold values η and γ, we simply considered the same values used in the paper (Kim et al., 2005) in the experimental evaluation of this method. The method described in (Park et al., 2015) utilizes the characteristics of 2D-Fourier transform and polar mapping for the effective classification of ISAR images. In this method, the ISAR images are transformed from spatial domain to frequency domain using 2D-

Fourier transform and polar mapping is applied on 2D-FT images to achieve rotation invariance. Then, in the classification phase, the test images are aligned with the trained images using simple correlation and the final classification result is obtained by applying simple nearest-neighbour classifier on the compressed trained and test images using 2D-PCA.

4.1. Conventional classification method

Conventional classification method depends on Euclidean distance between the images to find the class label of the input image. In the training phase, some ISAR images are selected from the data set for the training. The selected ISAR images are pre-processed using the method described in Section 3, class labels are assigned and are stored in the database called trained database. In the testing phase, test image is selected and pre-processed. Then, the Euclidean distance is calculated between the processed test image and the trained database. The class label of the trained image with which the smallest Euclidean distance is obtained with the test image is determined as its class label.

4.2. Performance evaluation

The performance of the proposed method is studied and compared against the conventional, polar mapping (Kim et al., 2005) and Fourier polar mapping (Park et al., 2015) schemes. The experimental analysis is carried out on two datasets, SynISAR (Kondaveeti, 2016) and dataset-2. SynISAR consisting of ISAR images of 7 aircraft models and dataset-2, our dataset, consists of ISAR images of 5 aircraft models. Fig. 9 depicts the ISAR images of aircrafts from the dataset SynISAR at arbitrary aspect angles.

2D-ISAR images of various aircraft models in the dataset-2 are synthesized from their basic 3D-CAD models. The images are generated over 1°–180° with 1° interval by the motion simulation of the aircrafts in counter-clockwise direction about yaw axis. The yaw motion is a clockwise or counter-clockwise movement of the nose of the aircraft about the axis perpendicular to both the wings of the aircraft and the plane in which the centre line of aircraft lies. Fig. 10 depicts the motion

of the aircraft in counter-clockwise direction about the yaw axis. The synthesized ISAR imagery simulate the rudimental silhouettes of the aircrafts in 2D images which proximate the ISAR imagery generated in real scenarios. More care has been taken in synthesizing the ISAR images to resemble the real ISAR imagery. All the algorithms are implemented with MATLAB programing and experiments are performed on Intel Core2 Duo 2.93 GHz CPU.

In the SynISAR, the number of ISAR images corresponding to each target is 181, and thus the whole data set includes 1267 ISAR images. Similarly dataset-2 contains 905 ISAR images of 5 aircrafts with 181 images corresponding to each target. The two datasets are clearly described in Table 1.

The experimental analysis on two datasets SynISAR (Kondaveeti, 2016) and dataset-2, is carried out separately and results are presented and discussed in the following subsections. To analyse the classification performance of the proposed method on dataset SynISAR, training database is built by uniform sampling of images of each target across 1°–180° with a difference of 5° yielding 252 images with 36 images corresponding to each target. The remaining 1015 images are used for testing purpose. Similarly for dataset-2, training database is built by uniform sampling of 36 images of each target yielding 180 images and the remaining 725 images are used for testing. In both datasets, 20% of the data is used for training and remaining 80% of data is used for testing. The ISAR images that are used for training are not considered for testing.

To make the classifier robust against the deformations in the ISAR images, the classifier in the proposed method is trained in such a way that the training data consists of ISAR imagery at different levels of distortions. The uniformly sampled 36 images of each target are divided into 5 sets having 8 images in first set and 7 images in each of the remaining 4 sets. The images in the first set are preprocessed with the global threshold ζ and area opening parameter λ, represented in the shape matrix form using MECSM representation and saved in the training database. The remaining four sets containing 7 images are initially preprocessed with varying the value of global threshold ζ by incrementing its value by a factor of 10–40 with an increment of a factor 10 for each set while keeping area opening parameter λ constant i.e. first set of the
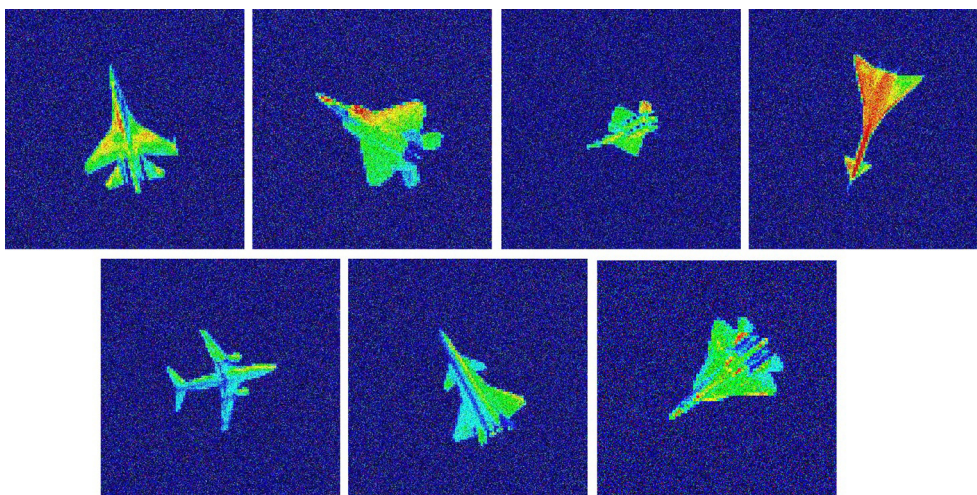
Figure 9 ISAR images of aircrafts from dataset SynISAR (Kondaveeti, 2016) at arbitrary aspect angles.
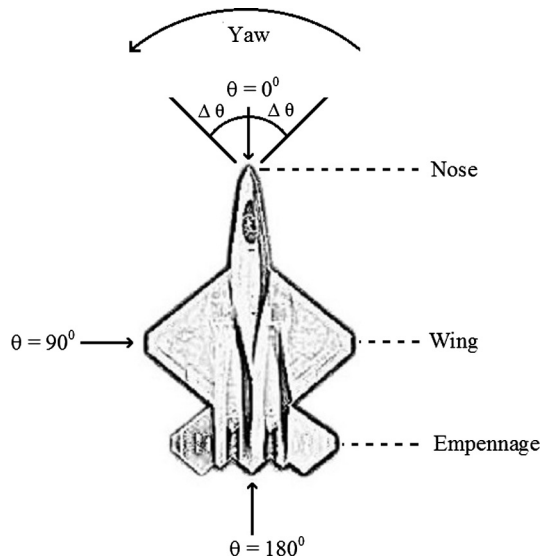
Figure 10 Yaw motion of an aircraft in counter-clockwise for dataset generation and for the sampling of training and test sets

remaining four sets of images is preprocessed with incremented global threshold ζ by a factor of 10 and the remaining three sets of images are preprocessed with global threshold ζ incremented by a factor of 20, 30 and 40 respectively. Next, the preprocessed images are represented in the shape matrix form using MECSM representation and saved in the training database. When the global threshold ζ value is incremented by a constant factor, the level of distortions and deformations increase in the ISAR images.

The experimental analysis is performed on the test data by considering the average correct classification rate, P_c. Correct classification rate, P_c is defined as the number of input images classified correctly over the number of input images given for the classification. P_c can be expressed as in Eq. (15)

$$P_c = \frac{\text{No. of correctly classified test images}}{\text{No. of test images given for the classification}} \quad (15)$$

The average value of the recognition rates obtained in ten observations is considered to avoid classification errors.

The experimental analysis is carried out separately on dataset SynISAR and dataset-2 by varying the blur, Signal to Noise Ratio SNR_{dB} and level of deformations in the shapes of the targets in the test ISAR images to simulate the real scenarios. In the experimentation, the test ISAR images are down-scaled, rotated arbitrarily between the angles $-\pi$ to π and translated across the range $[\pm 100, \pm 100]$. Here, scale refers to the area occupied by a target in the ISAR image. Similarly, rotation and translation represent the orientation and position of the

target in the ISAR image. Initially, all experiments are carried out by keeping the scale factor constant and then, the same experiments are carried out with varying the scale between 1 and $1/\sqrt{2}$ of the test ISAR images. Two variants of the method (Park et al., 2015) are used in the experimentation. First variant is without up-sampling the images and the second one is with up-sampling the images by zero-padding before applying 2D-FT. In all the methods, same number of points 100×100 are considered for the polar quantization of the targets for consistency i.e. $N_\theta = 100$ and $N_r = 100$ in case of the methods (Kim et al., 2005 and Park et al., 2015) and size of the shape matrix is considered as 100×100 in case of the proposed method.

In all the experiments, the proposed method performed consistently as the proposed classification method depends on the binary representation of shape of the targets rather than depending the true grey value representation of the target. The scenarios considered for the experimental analysis, performances of the three classification methods and associated discussions are presented in the following sub-sections in detail.

Experiment – 1

In this experiment, the performances of the four methods are compared when the SNR_{dB} is varied between 5 and 30 dB with an increment of 5 dB without changing the scale of the test image. Fig. 11 depicts the performances of the four methods.

All the four methods are performing nearly similar at SNR_{dB} values between 10 and 30 dB. However, the robustness of the proposed method can be observed when ISAR images are corrupted by noise having SNR_{dB} below 2 dB. Next experiment reveals the strength of the proposed method.
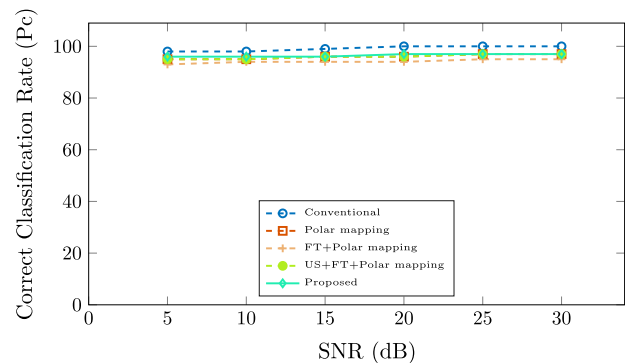
Figure 11 Comparison of accuracies of the proposed method against conventional method, polar mapping method (Kim et al., 2005) and two variants of Fourier Polar mapping method (Park et al., 2015) on the dataset SynISAR when the SNR_{dB} is varied between 5 and 30 dB with an increment of 5 dB.

Table 1	Description of datasets.				
Dataset	Details				
	Total No. of images	No. of classes	No. of instances in each class	No. of orientations	Size of image
SynISAR (Kondaveeti, 2016)	1267	7	181	180	300×300
Dataset-2	905	5	181	180	300×300

Experiment – 2

In this experiment, the performances of the four methods are compared when the SNR_{dB} is varied between 0.25 and 1.5 dB with an increment of 0.25 dB without changing the scale of the test image. Fig. 12 depicts the performances of the four methods. At higher SNR_{dB} all the four methods are performing equally good. But, when SNR_{dB} below 2 dB is considered the conventional and polar mapping methods failed utterly and the performance of the fourier polar mapping method dropped drastically. Low SNR causes lose of discriminative information to classify the targets in case of both conventional and polar mapping methods. Changes in the pixel intensity values

Figure 12 Comparison of accuracies of the proposed method against conventional method, polar mapping method (Kim et al., 2005) and two variants of Fourier Polar mapping method (Park et al., 2015) on the dataset SynISAR when the SNR_{dB} is varied between 0.25 and 1.5 dB with an increment of 0.25 dB.

also causes abrupt changes in the Fourier spectrum as noise that corrupted the images is not periodic. Simple noise removal process described in the polar mapping (Kim et al., 2005) and Fourier polar mapping (Park et al., 2015) methods can not cope up with higher levels of noise. The outliers remained in the preprocessed image highly affect the construction of the imaginary polar grid which in turn worsens the classifier accuracy in case of (Kim et al., 2005). The proposed method is performing constantly even at the low SNR values as the noise removal procedure described in the proposed method is robust against the noise levels and outliers.

Experiment – 3

In this experiment, the performances of the four methods are compared at various levels of image blur at SNR is 25 dB. In real scenarios, unsuccessful motion compensation in the generation of ISAR images of moving targets causes blur effect. To investigate the performances of the four methods against the blur, 2D- Finite Impulse Response (FIR) filter is applied to the ISAR images. An FIR filter with constant weight W is often referred as 2D-running average filter with low-pass frequency response which causes blur effect. The response of 2D-FIR can be expressed as in Eq. (16)
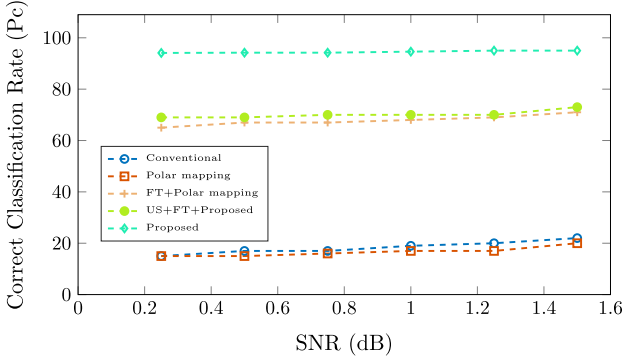
$$I_{blur}(x_p, y_q) = \sum_{i=-L}^{L}\sum_{j=-L}^{L} W_{i,j} I(x_{p-i}, y_{q-j}) \tag{16}$$

where $I_{blur}(x_p, y_q)$ is the blurred ISAR image after applying 2D-FIR filter with filter weight $W_{i,j}$ on the original ISAR image $I(x_p, y_q)$.

The filter weight is given by $W_{i,j} = 1/L^2$ where $i = -L, \ldots, L, j = -L, \ldots, L$ and L is the order of the filter.

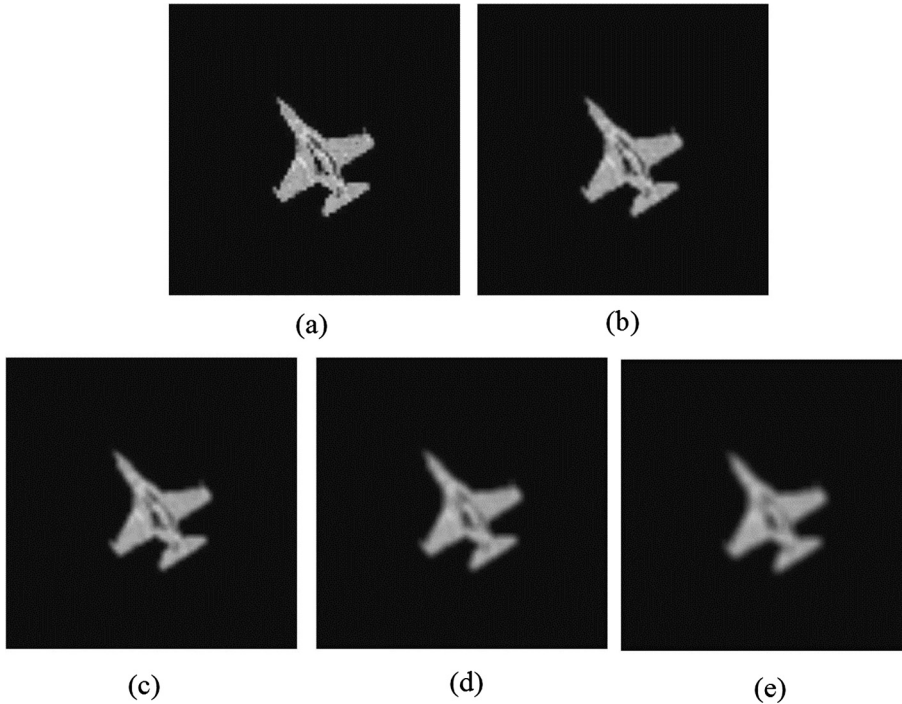**Figure 13** Comparison of the images after applying 2D-FIR at different filter orders on the ISAR image of aircraft at an arbitrary aspect angle. (a) Blurred ISAR image when filter order, $L = 3$; (b) Blurred image ISAR when filter order, $L = 5$; (c) Blurred ISAR image when filter order, $L = 7$; (d) Blurred ISAR image when filter order, $L = 9$; (e) Blurred ISAR image when filter order, $L = 11$;

Increase in the value of L causes more blur effect which reduces the scattering information of the target.

To carry out the classification experimentation, test images are blurred by 2D-FIR filter (16) in addition to rotation and translation. The process of testing has been performed at SNR_{dB} is 25 dB at different filter orders $L = 3, 5, 7, 9, 11$. Fig. 13 shows the effect of applying 2D-FIR at different filter orders on the ISAR image of aircraft at an arbitrary aspect angle. Fig. 13(a), (b), (c), (d) and (e) represent the responses of 2D-FIR at the filter orders $L = 3, 5, 7, 9, 11$ respectively. The obtained average P_c at specified value of L is used to produce the comparative results.

Fig. 14 depicts the performance of the four methods against the variations in blur levels when SNR is 25 dB and the test image is not down-scaled. The conventional method is giving unsatisfactory results against all the filter order variations because this method is highly affected by blur as it depends on the original scatter response values of the ISAR images. The polar mapping method is robust up to $L = 7$ and the average P_c value is dropping off drastically with higher filter orders 9 and 11. As the polar mapping method also depends on the original scatter response values of the ISAR images to generate the feature vector, the accuracy of this method decreases with the loss of scatter response due to the blur caused by higher filter orders. The performance of the Fourier polar mapping method is decreased with the increase in the level of blur as the Fourier spectrum of the ISAR images depends on the pixel intensities in the spatial domain. But, however, the proposed method performs steadily with blur caused by different filter orders as this method depends on the shape details rather than the scatter response values.

Experiment – 4

In this experiment, the performances of the four methods are compared when the SNR_{dB} is varied between 5 and 30 dB with an increment of 5 dB and test image is down-scaled. The proposed and polar mapping methods are robust against the scale changes as the feature vectors generated by the both methods are scale invariant. The performance of the conventional method degrades with the down-scaled ISAR images due to lack of scale invariant mechanism. Fig. 15 represents the performance variations of the four methods with the scale changes in the ISAR test images.
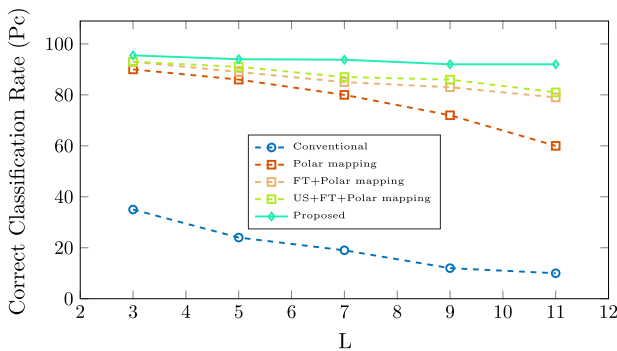

Figure 14 Comparison of accuracies of the proposed method against conventional method, polar mapping method (Kim et al., 2005) and two variants of Fourier Polar mapping method (Park et al., 2015) on the dataset SynISAR with the image blurring when SNR_{dB} is 25 dB.

Figure 15 Comparison of accuracies of the proposed method against conventional method, polar mapping method (Kim et al., 2005) and two variants of Fourier Polar mapping method (Park et al., 2015) on the dataset SynISAR when the SNR_{dB} is varied between 5 and 30 dB with an increment of 5 dB and test image is down-scaled.

Experiment – 5

In this experiment, the performances of the four methods are compared when the SNR_{dB} is varied between 0.25 and 1.5 dB with an increment of 0.25 dB and test image is down-scaled. The performances of the four methods are depicted in Fig. 16.

Experiment – 6

In this experiment, the performances of the four methods against the variations in blur levels are compared when the SNR_{dB} is 25 dB and test image is down-scaled. Fig. 17 depicts the performances of the four methods when the test image is blurred and down-scaled.

Experiment – 7

In this experiment, the performances of the four methods are compared when the global threshold value, ζ is varied by incrementing its value by a factor of 10–40 with an increment of a factor 10 when the SNR_{dB} is 25 dB varying scales of test image. The global threshold value, ζ obtained by minimizing intra-

Figure 16 Comparison of accuracies of the proposed method against conventional method, polar mapping method (Kim et al., 2005) and two variants of Fourier Polar mapping method (Park et al., 2015) on the dataset SynISAR when the SNR_{dB} is varied between 0.25 and 1.5 dB with an increment of 0.25 dB and test image is down-scaled.

Figure 17 Comparison of accuracies of the proposed method against conventional method, polar mapping method (Kim et al., 2005) and two variants of Fourier Polar mapping method (Park et al., 2015) on the dataset SynISAR with the image blurring when SNR_{dB} is 25 dB and test image is down-scaled.
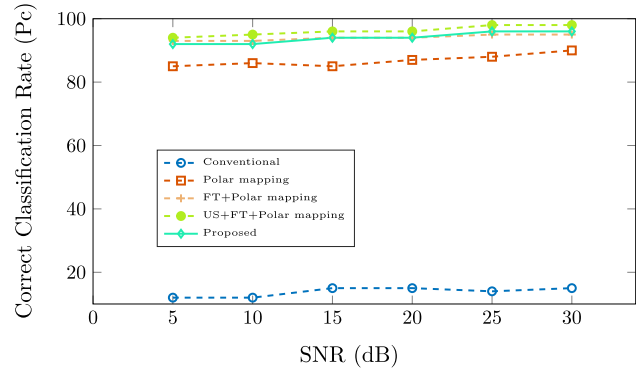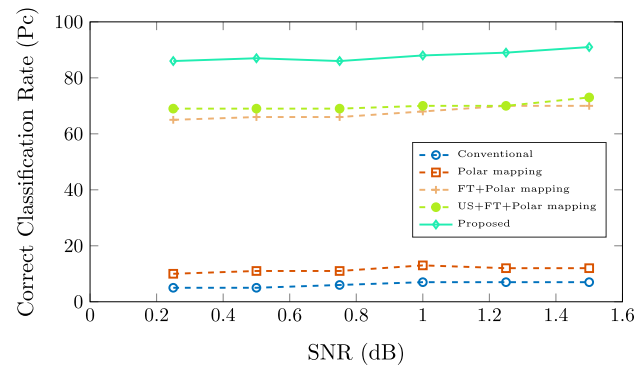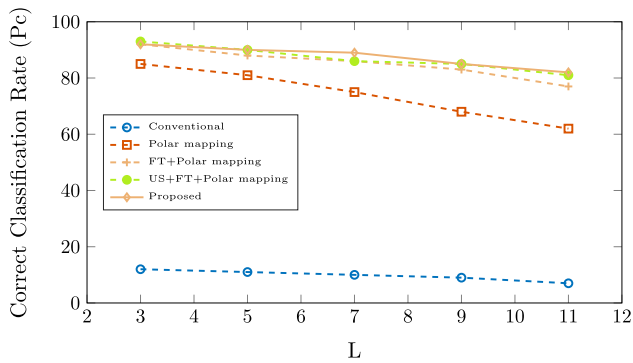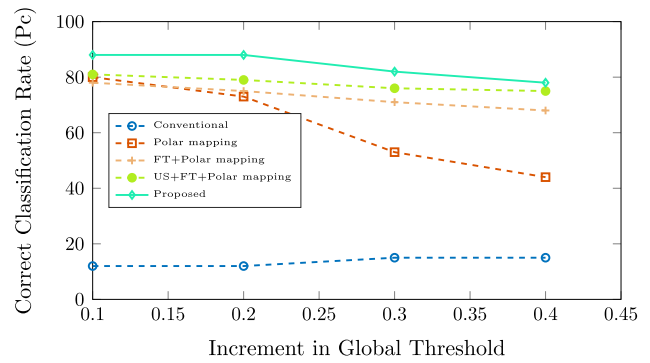

Figure 19 Comparisons of accuracies of the proposed method against conventional method, polar mapping method and two variants of Fourier Polar mapping method on the dataset SynISAR when the global threshold value, ζ is varied by incrementing its value by a factor 10–40 with an increment of 10 when the SNR_{dB} is 25 dB.

class variations plays an important role in removing the noise while preserving the target's information. When the value of the ζ is increased by a constant factor, influential details of the targets are vanished along with noise which cause breaks in the silhouettes of the targets. Fig. 18 depicts the effect of incrementing the global threshold by a factor 10. Fig. 18(a) represents the preprocessed ISAR images of two different aircraft targets at arbitrary angles with a global threshold value, ζ. The parameter of area opening operation, λ is considered as 10 for this experimentation. Segmentation using ζ removes noise successfully while preserving most of the influential details of the target. But, when the ζ value is incremented by a factor 10, 20, 30 and 40 the images obtained are represented in the sub-figures (b), (c), (d) and (e) respectively.

The robustness of the four methods against the loss of influential information can be observed from Fig. 19. The mecha-

nism described in the proposed method makes it robust against the deformations and discontinuities in the shape of the targets. The performances of variants of Fourier polar images are slightly decreased due to glitches in the spectrum caused by the breaks in the super structure of the targets.

The experiments 1–7 are carried out on the dataset SynISAR till now. The same experiments are repeated on dataset-2 to test the effectiveness of the proposed method on other variants of aircraft models. The results obtained are presented in Tables 2–8.

The execution times (in seconds) of the proposed method against conventional method, polar mapping method and two variants of Fourier Polar mapping method on datasets SynISAR (Kondaveeti, 2016) and dataset-2 are presented in Table 9. The execution times are calculated programmatically
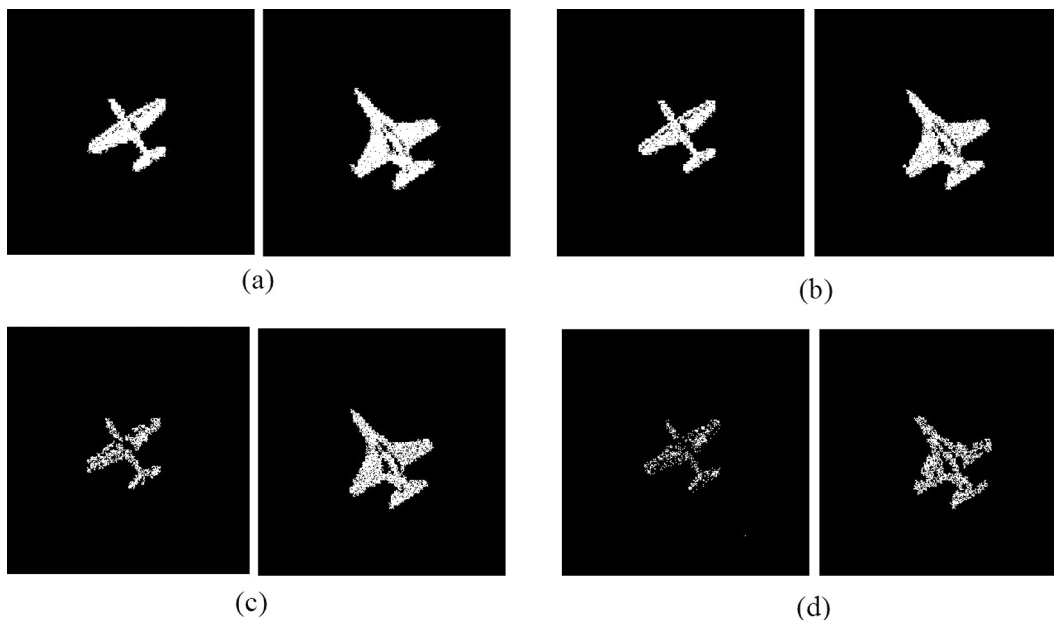
Figure 18 Comparison of images obtained from the preprocessing step by incrementing the value of the global threshold, ζ by a factor of 10–40 with an increment of a factor 10.

Table 2   Comparisons of accuracies of the proposed method against conventional method, polar mapping method (Kim et al., 2005) and two variants of Fourier Polar mapping method (Park et al., 2015) on dataset-2 when the SNR_{dB} is varied between 5 and 30 dB with an increment of 5 dB without down-scaling the test images.

SNR_{dB}	Experiment – 1				
	Conventional	Polar mapping (Kim et al., 2005)	FT + polar mapping (Park et al., 2015)	US + FT + polar mapping (Park et al., 2015)	Proposed
5	98.3	94.8	93.2	94.9	96.3
10	98.5	95.3	93.8	95.5	96.5
15	98.5	95.8	94.1	95.8	96.5
20	99.5	96	94.2	96.3	96.8
25	99.8	97.2	94.8	97.2	97
30	100	97.5	95.2	98.2	97.2

Table 3   Comparison of accuracies of the proposed method against conventional method, polar mapping method (Kim et al., 2005) and two variants of Fourier Polar mapping method (Park et al., 2015) on dataset-2 when the SNR_{dB} is varied between 0.25 and 1.5 dB with an increment of 0.25 dB without down-scaling the test images.

SNR_{dB}	Experiment – 2				
	Conventional	Polar mapping (Kim et al., 2005)	FT + polar mapping (Park et al., 2015)	US + FT + polar mapping (Park et al., 2015)	Proposed
0.25	13.2	15.3	65.3	68.9	93.8
0.5	16.3	15.8	66.7	68.9	94
0.75	16.5	16.2	66.8	69.6	94.3
1	19	17.2	67.6	69.8	94.8
1.25	21.4	17.7	69.5	70.1	95.6
1.5	22	20.6	70.6	72.5	95.8

Table 4   Comparison of accuracies of the proposed method against conventional method, polar mapping method (Kim et al., 2005) and two variants of Fourier Polar mapping method (Park et al., 2015) on dataset-2 when the SNR_{dB} is varied between 5 and 30 dB with an increment of 5 dB with down-scaling the test images.

SNR_{dB}	Experiment – 4				
	Conventional	Polar mapping (Kim et al., 2005)	FT + polar mapping (Park et al., 2015)	US + FT + polar mapping (Park et al., 2015)	Proposed
5	11.8	84.5	92.6	94.3	91.5
10	12.5	86	93.4	95.5	92.6
15	14.5	86.5	94.2	95.7	94.5
20	96.8	15.8	94.2	96.4	95.5
25	97	15.8	94.6	97.8	96.3
30	17	89.8	95.1	98.3	97.1

Table 5   Comparison of accuracies of the proposed method against conventional method, polar mapping method (Kim et al., 2005) and two variants of Fourier Polar mapping method (Park et al., 2015) on dataset-2 when the SNR_{dB} is varied between 0.25 and 1.5 dB with an increment of 0.25 dB with down-scaling the test images.

SNR_{dB}	Experiment – 5				
	Conventional	Polar mapping (Kim et al., 2005)	FT + polar mapping (Park et al., 2015)	US + FT + polar mapping (Park et al., 2015)	Proposed
0.25	5.3	10.5	64.8	68.9	86.5
0.5	5.8	11.4	66.1	68.9	87.2
0.75	6.8	11.9	66.4	69.4	88.4
1	7.9	15.8	67.8	69.6	89.8
1.25	8.3	17.9	69.6	70.1	90.3
1.5	9.5	20.6	70.3	72.7	91.5

Table 6 Comparison of accuracies of the proposed method against conventional method, polar mapping method (Kim et al., 2005) and two variants of Fourier Polar mapping method (Park et al., 2015) on dataset-2 with the image blurring at various filter orders L when SNR_{dB} is 25 dB without down-scaling the test images.

| L | Experiment – 3 | | | | |
	Conventional	Polar mapping (Kim et al., 2005)	FT + polar mapping (Park et al., 2015)	US + FT + polar mapping (Park et al., 2015)	Proposed
3	17	89	92.9	93.1	95.6
5	15.5	85.5	89.3	90.6	93.8
7	14.3	81	85.4	87.3	93.3
9	13.5	73.5	83.1	85.7	91.5
11	10.4	61.4	78.6	81.1	91

Table 7 Comparison of accuracies of the proposed method against conventional method, polar mapping method (Kim et al., 2005) and two variants of Fourier Polar mapping method (Park et al., 2015) on dataset-2 with the image blurring at various filter orders L when SNR_{dB} is 25 dB with down-scaling the test images.

| L | Experiment – 6 | | | | |
	Conventional	Polar mapping (Kim et al., 2005)	FT + polar mapping (Park et al., 2015)	US + FT + polar mapping (Park et al., 2015)	Proposed
3	12.6	85.6	91.9	92.6	92.7
5	11.3	80.4	88.3	90.2	90.5
7	10.5	75.6	85.6	86.5	89.5
9	9.7	68.5	83.1	85.4	85.3
11	7.2	62.5	77.5	80.9	82.2

Table 8 Comparisons of accuracies of the proposed method against conventional method, polar mapping method (Kim et al., 2005) and two variants of Fourier Polar mapping method (Park et al., 2015) on dataset-2 when the global threshold value, ζ is varied by incrementing its value by a factor 10–40 with an increment of 10 when the SNR_{dB} is 25 dB.

| Threshold increment factor | Experiment – 7 | | | | |
	Conventional	Polar mapping (Kim et al., 2005)	FT + polar mapping (Park et al., 2015)	US + FT + polar mapping (Park et al., 2015)	Proposed
10	13.5	80.3	78.3	80.6	88.6
20	12.8	73.5	74.9	78.9	88.2
30	11.3	64.8	70.6	76.2	82.7
40	10.2	54.2	68.3	74.9	77.5

Table 9 Comparisons of execution times (in sec) of the proposed method against conventional method, polar mapping method (Kim et al., 2005) and two variants of Fourier Polar mapping method (Park et al., 2015) on datasets SynISAR (Kondaveeti, 2016) and dataset-2.

Size of the test image	Conventional	Polar mapping	FT + polar mapping	US + FT + polar mapping	Proposed
SynISAR					
150 × 150	2.33	4.87	5.15	5.82	4.22
200 × 200	2.96	5.34	6.95	7.46	5.28
250 × 250	3.75	7.66	8.21	8.83	7.33
300 × 300	4.83	8.28	9.24	10.25	8.14
Dataset-2					
150 × 150	1.68	3.47	3.71	4.23	3.04
200 × 200	2.02	3.93	4.96	5.11	3.76
250 × 250	2.83	5.53	5.71	6.04	5.23
300 × 300	3.51	6.26	6.89	7.46	5.94

using the stop watch function, to verify the computational efficiency of the proposed method against the existing methods. Execution times of each method is calculated as average of 50 observations to avoid computational errors. This analysis is carried out by varying the blur, Signal to Noise Ratio SNRdB and level of deformations in the shapes of the targets in the test ISAR images. Eventhough the size of test image is varied, same number of points 100×100 are considered for the polar quantization of the targets for consistency i.e. size of the shape matrix is considered as 100×100 in case of the proposed method and $N_\theta = 100$ and $N_r = 100$ in case of the methods (Kim et al., 2005 and Park et al., 2015).

5. Conclusion

In military surveillance, accuracy of the automatic target detection and classification mechanisms play a crucial role in making tactic decisions in hostile environments. In this paper robust ISAR image classification method is proposed for Automatic Target Classification in real battle field scenarios. The proposed classification method depends on the Minimum Circumscribed Circle based Shape Matrix (MECSM) representation of the targets for the classification. The MECSM representation addresses the limitations in the conventional shape matrix representation and also avoids the extraneous interpolations which does not carry any discriminative information for the classification. The MECSM depends on centre of the Minimum Circumscribed Circle to generate the shape matrix which makes it robust against the discontinuities and deformations in the shape of the targets. Experimental results show that the proposed method is giving reliable performance and better accuracy than the existing ISAR classification schemes in various experimental scenarios such as variation in SNR_{dB}, blur and level of deformations in the shapes of the targets.

References

Bachmann, C., Musman, S., Schultz, A., 1992. Lateral inhibition neural networks for classification of simulated radar imagery. Int Joint Conf. Neural Netw. 2, 115–120.

Botha, E., 1994. Classification of aerospace targets using super-resolution ISAR images. Proc. IEEE S. Afr. Symp. Commun. Signal Process., 138–145

Brett, B., 1997. Some issues in inverse synthetic aperture radar image reconstruction. Inverse Problems 13 (3), 571–584.

Chen, C., Anderson, H., 1980. Target motion induced radar imaging. IEEE Trans AES AES-16 (1), 2–14.

Chen, V.C., 2014. Inverse Synthetic Aperture Radar Imaging Principles, Algorithms and Applications. The Institution of Engineering and Technology, Stevenage, URL: < http://cds.cern.ch/record/1953312 > .

Franceschetti, G., Lanari, R., 1999. Synthetic Aperture Radar Processing. CRC Press.

Gadelmawla, E., 2010. Simple and efficient algorithms for roundness evaluation from the coordinate measurement data. Measurement 43 (2), 223–235.

Goshtasby, A., 1985. Description and discrimination of planar shapes using shape matrices. IEEE Trans. Pattern Anal. Mach. Intell. 7 (6), 738–743.

Jaccard, P., 1901. Distribution de la flore alpine dans le bassin des dranses et dans quelques rgions voisines. Bull. Soc. Vaudoise Sc. Nat. 37, 241–272.

Jain, A., Duin, R., Mao, J., 2000. Statistical pattern recognition: a review. IEEE Trans. Pattern Anal. Mach. Intell. 22 (1), 4–37.

Kim, K., Seo, D., Kim, H., 2005. Efficient classification of ISAR images. IEEE Trans. Antennas Propagat. 53 (5), 1611–1621.

Kondaveeti, H., 2016. SynISAR. doi: http://dx.doi.org/10.5281/zenodo.48002.

Kondaveeti, H., Vatsavayi, V., 2016. Robust ISAR image classification using abridged shape matrices. In: International Conference on Emerging Trends in Engineering, Technology and Science. IEEE Press (in press).

Kozma, A., Walker, J., Jones, H., Poggio, E., 1984. Developments in radar imaging. IEEE Trans Aerospace and Electronic Systems AES-20 (4), 363–400.

Maki, A., Fukui, K., Onoguchi, K., Maeda, K., 2001. Isar image analysis by subspace method: Automatic extraction and identification of ship profile. In: 11th International Conference on Image Analysis and Processing. pp. 523–528.

Musman, S., Kerr, D., Bachmann, C., 1996. Automatic recognition of ISAR ship images. IEEE Trans. Aerosp. Electron. Syst. 32 (4), 1392–1404.

Nuthalapati, R.M., 1992. High resolution reconstruction of isar images. IEEE Transactions on Aerospace and Electronic Systems 28 (2), 462–472. http://dx.doi.org/10.1109/7.144572.

Otsu, N., 1979. A threshold selection method from gray level histograms. IEEE Trans Syst. Man Cybernet. 9, 62–66.

Ozdemir, C., 2012. Inverse Synthetic Aperture Radar Imaging with MATLAB Algorithms. Wiley Series in Microwave and Optical Engineering. J. Wiley & Sons, Hoboken, NJ, URL: < http://cds.cern.ch/record/1555083 > .

Park, S., Jung, J., Kim, S., Kim, K., 2015. Efficient classification of ISAR images using 2d fourier transform and polar mapping. IEEE Trans. Aerosp. Electron. Syst. 51 (3), 1726–1736.

Rosenbach, K., Schiller, J., 1995. Identification of aircraft on the basis of 2-d radar images. IEEE Int. Radar Conf. Record, 405–409.

Saidi, M., Daoudi, K., Khenchaf, A., Hoeltzener, B., Aboutajdine, D., 2009. Automatic target recognition of aircraft models based on ISAR images. IEEE Int. Geosci. Remote Sens. Symp., 685–688

Skinner, J., Kent, B., Wittmann, R., Mensa, D., Andersh, D., 1998. Normalization and interpretation of radar images. IEEE Trans. Antennas Propagat. 46 (4), 502–506.

Sullivan, Roger J., 2000. Microwave Radar: Imaging and Advanced Concepts. Artech House, Boston, London.

Tang, N., Gao, X.Z., Li, X., 2012. Target classification of ISAR images based on feature space optimisation of local non-negative matrix factorisation. IET Signal Processing 6 (5), 494–502. http://dx.doi.org/10.1049/iet-spr.2011.0286.

Taza, A., Suen, C., 1989. Discrimination of planar shapes using shape matrices. IEEE Trans. Syst. Man Cybernet. 19 (5), 1281–1289.

Zeljkovic, V., Li, Q., Vincelette, R., Tameze, C., Liu, F., 2010. Automatic algorithm for inverse synthetic aperture radar images recognition and classification. IET Radar, Sonar Navigation 4 (1), 96–109. http://dx.doi.org/10.1049/iet-rsn.2009.0112.